Free vibration analysis of functionally graded triply periodic minimal surface plates using a first order shear deformation theory and meshfree method

P. Phung-Van[1], P.T. Hung[2], H. Nguyen-Gia[1], H. Nguyen-Xuan[3,*]

[1]Faculty of Civil Engineering, HUTECH University, Ho Chi Minh City, Vietnam
[2]Faculty of Civil Engineering, Ho Chi Minh City University of Technology and Education, Ho Chi Minh City, Vietnam
[3]CIRTECH Institute, HUTECH University, Ho Chi Minh City, Vietnam

*Corresponding Author: H. Nguyen-Xuan (Email: ngx.hung@hutech.edu.vn), P. Phung-Van (pv.phuc86@hutech.edu.vn)

Abstract. *This paper explores a free vibration analysis of functionally graded triply periodic minimal surface plates using a first order shear deformation theory in conjunction with moving Kriging meshfree method. The FG-TPMS plates are modeled the same as porous structures with three different patterns (Primitive, Gyroid, and wrapped package-graph) and six different volume distributions for each pattern. Employing a fitting method based on a two-phase piece-wise function, the mechanical properties of the FG-TPMS plates are determined. The governing equations for the FG-TPMS plates are established using the virtual work principle and subsequently solved using the moving Kriging meshfree method. The study encompasses FG-TPMS square and circular plate, examining the natural frequency of the FG-TPMS plates with various length-to-thickness ratios, TPMS types, volume distributions, and boundary conditions.*

Keywords: **First order shear deformation theory, Moving Kriging meshfree method, Triply periodic minimal surface, Cellular materials**

1. Introduction

In recent years, conventional cellular structures like honeycombs, lattice structures, and foam materials have been extensively studied for their mechanical properties [1, 2]. Minimal surfaces, which have zero average curvature, have attracted interest in research communities. Triply periodic minimal surface structures, which are characterized by smooth and continuous surfaces derived from mathematical methods, have zero mean curvatures at every point. Various TPMS structures including Primitive, Gyroid, and IWP can be generated using different mathematical models [3]. Additive manufacturing technology has emerged as a promising approach for fabricating TPMS structures, enabling researchers to explore their mechanical characteristics. Numerical simulations and experimental studies have been conducted to investigate deformation processes and energy absorption performance of TPMS structures produced through additive manufacturing technology [4].

To enhance the mechanical properties of TPMS structures, various types of FG-TPMS structures have been introduced in recent stud-

ies. These structures include the hybridization of different unit cell geometries [5] and gradient volume fraction [6,7]. Researchers have designed FG structures by incorporating z-value terms into the formulas, resulting in gradient Primitive and Gyroid structures [3,8]. The FG structures based on TPMS solely along the z-axis have been manufactured, demonstrating improved energy absorption capacity compared to uniform structures [9]. Different types of FG-TPMS structures [10] have been investigated, revealing a combination of stretching- and bending-dominated deformations. Deformation behaviors of one-dimensional FG-Primitive structures have been studied under various loading directions, indicating superior energy absorption capability only when the loading and the gradient directions are parallel [11]. On the other hand, an analysis of the biological and mechanical properties of graded porous scaffolds based on refined Primitive and Gyroid, Diamond, and IWP TPMS types was conducted by Ma *et al.* [12]. Wang *et al.* [13] guided an assessment of the mechanical properties, morphology, permeability, and cell growth of gradient TPMS structures. The failure mechanism of Gyroid structures under compressive loadings, identifying the formation of shear bands as the major failure mechanism was investigated by Keshavarzan *et al.* [14]. Afshar *et al.* [15] explored the deformation mechanism of TPMS with graded porosities, revealing that stretching-dominated structures exhibited superior mechanical properties compared to bending-dominated structures. Qiu *et al.* [16] introduced mechanical properties of three-dimensional FG-TPMS structures. Moreover, the free vibration and buckling analyses of FG-TPMS beams were performed by Viet and Zaki [17]. Specially, Nguyen-Xuan *et al.* [18] developed a higher order shear deformation model for FG-TPMS plates by using a fitting technique. In addition, by using the same model, an analysis of FG-TPMS microplates based on the modified couple stress theory was performed in [19].

This study aims to develop the moving Kriging meshfree method based on FSDT for FG-TPMS plates. The obtained results are compared to the reference results [18], which used isogeometric analysis (IGA) and HSDT. Be-

sides, IGA successfully applied to multi-physics problems [20–23]. A comparison between the two methods reveals several advantages of the present method: (i) The meshfree approximate functions are constructed directly using nodal data in global Cartesian coordinates, so the present method is good for the complex geometry; (ii) displacement and stresses can be computed directly at arbitrary points in physical space, avoiding the need for calculations in natural coordinates as in IGA. Furthermore, boundary conditions are enforced directly at nodes, similar to finite element method, instead of employing penalty methods or Lagrange multipliers used in other meshfree methods. The moving Kriging meshfree method was firstly proposed and developed by Gu [24] to apply the 2-dimesional problem. Subsequently, this method has been further developed and successfully utilized for the analysis of plates [25–31] and microplates [32–34].

2. Basic equations

2.1. Mechanical properties of FG-TPMS materials

Three types of FG-TPMS plate models can be considered: Primitive, Gyroid, and I-graph and wrapped package-graph (IWP), as plotted in Figure 1. The TPMS geometry defines the characteristics of the sheet-based solid type as follows [18]
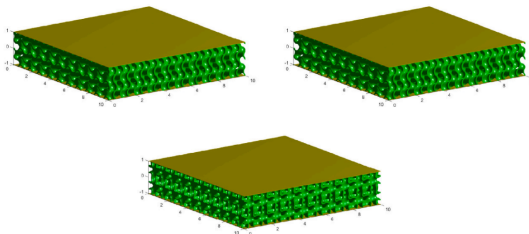
Fig. 1: Based on pattern I, three different types of FG-TPMS plates [18].

Primitive $\Xi = \cos\left(\omega_1 x\right) + \cos\left(\omega_2 y\right) + \cos\left(\omega_3 z\right)$

Gyroid $\Xi = \sin\left(\omega_1 x\right)\cos\left(\omega_2 y\right) + \sin\left(\omega_2 y\right)\cos\left(\omega_3 z\right) + \sin\left(\omega_3 z\right)\cos\left(\omega_1 x\right)$

IWP $\Xi = 2\left(\cos\left(\omega_1 x\right)\cos\left(\omega_2 y\right) + \cos\left(\omega_2 y\right)\cos\left(\omega_3 z\right) + \cos\left(\omega_3 z\right)\cos\left(\omega_1 x\right)\right)$
$- \left(\cos\left(2\omega_1 x\right) + \cos\left(2\omega_2 y\right) + \cos\left(2\omega_3 z\right)\right)$

$$\tag{1}$$

where

$$\omega_i = \frac{2\pi n_i}{l_i},\ i = 1, 2, 3 \tag{2}$$

in which is the number of unit cell and is their lengths. This research uses the fitting curve model reported in [18] that describes the volume ratio as follows

$$V = \frac{V^{TPMS}}{V^m} \tag{3}$$

where V^{TPMS} is the total volume of TPMS cells and V^m is the base material. Additionally, the volume ratio function can be described by

$$V = \left\{ \begin{array}{l} \left(V_{\max} - V_{\min}\right)\left(\frac{z}{h} + \frac{1}{2}\right)^n + V_{\min}\ \text{Pattern I} \\ \left(V_{\max} - V_{\min}\right)\left(1 - \cos\left(\frac{\pi z}{h}\right)\right)^n + V_{\min}\ \text{Pattern II} \end{array} \right. \tag{4}$$

2.2. Kinematics of plate

Based on FSDT, the displacement fields of an arbitrary point positioned on the plate can be written by

$$\hat{\mathbf{u}}\left(x, y, z\right) = \mathbf{u}^1\left(x, y\right) + z\mathbf{u}^2\left(x, y\right) \tag{5}$$

where

$$\hat{\mathbf{u}} = \left\{ \begin{array}{c} \hat{u} \\ \hat{v} \\ \hat{w} \end{array} \right\};\ \mathbf{u}^1 = \left\{ \begin{array}{c} u \\ v \\ w \end{array} \right\};\ \mathbf{u}^2 = \left\{ \begin{array}{c} \psi_x \\ \psi_y \\ 0 \end{array} \right\} \tag{6}$$

in which u, v and w are the in-plane and transverse displacements, respectively; ψ_x and ψ_y are two rotations of the y-z, x-z planes, respectively.

Bending and shear strain components are defined as

$$\begin{array}{l} \boldsymbol{\varepsilon} = \left\{ \begin{array}{ccc} \varepsilon_{xx} & \varepsilon_{yy} & \gamma_{xy} \end{array} \right\}^{\mathrm{T}} = \boldsymbol{\varepsilon}^1 + z\boldsymbol{\varepsilon}^2 \\ \boldsymbol{\gamma} = \left\{ \begin{array}{cc} \gamma_{xz} & \gamma_{yz} \end{array} \right\}^{\mathrm{T}} = \boldsymbol{\varepsilon}^s \end{array} \tag{7}$$

where

$$\boldsymbol{\varepsilon}^1 = \left\{ \begin{array}{c} u_{,x} \\ v_{,y} \\ u_{,y} + v_{,x} \end{array} \right\};\boldsymbol{\varepsilon}^2 = \left\{ \begin{array}{c} \psi_{x,x} \\ \psi_{y,y} \\ \psi_{x,y} + \psi_{y,x} \end{array} \right\}$$

$$\boldsymbol{\varepsilon}^s = \left\{ \begin{array}{c} w_{,x} + \psi_x \\ w_{,y} + \psi_y \end{array} \right\} \tag{8}$$

A constitutive equation for linear elasticity solids under plane stress is given by

$$\left\{ \begin{array}{c} \sigma_{xx} \\ \sigma_{yy} \\ \tau_{xy} \\ \tau_{xz} \\ \tau_{yz} \end{array} \right\} = \left[\begin{array}{ccccc} \frac{E}{1-(\nu)^2} & \frac{\nu E}{1-(\nu)^2} & 0 & 0 & 0 \\ \frac{\nu E}{1-(\nu)^2} & \frac{E}{1-(\nu)^2} & 0 & 0 & 0 \\ 0 & 0 & G & 0 & 0 \\ 0 & 0 & 0 & G & 0 \\ 0 & 0 & 0 & 0 & G \end{array} \right] \left\{ \begin{array}{c} \varepsilon_{xx} \\ \varepsilon_{yy} \\ \gamma_{xy} \\ \gamma_{xz} \\ \gamma_{yz} \end{array} \right\} \tag{9}$$

where E, G and v are the Young's modulus, shear modulus and Poisson's ratio of FG-TPMS materials, respectively.

The values in Table 1 are calculated and listed based on the fixed data model [18].

Tab. 1: Mechanical properties of FG-TPMS materials

TPMS	Mechanical properties		V
Primitive	$E = E^m$	$0.317V^{1.264}$	$V \leq 0.25$
		$1.007V^{2.006} - 0.007$	$V > 0.25$
	$G = G^m$	$0.705V^{1.189}$	$V \leq 0.25$
		$0.953V^{1.715} + 0.047$	$V > 0.25$
	$v =$	$0.314e^{-1.004V} + 0.119$	$V \leq 0.55$
		$0.152V^2 - 0.235V + 0.383$	$V > 0.55$
Gyroid	$E = E^m$	$0.596V^{1.467}$	$V \leq 0.45$
		$0.962V^{2.351} + 0.038$	$V > 0.45$
	$G = G^m$	$0.777V^{1.544}$	$V \leq 0.45$
		$0.973V^{1.982} + 0.027$	$V > 0.45$
	$v =$	$0.192e^{-1.349V} + 0.202$	$V \leq 0.50$
		$0.402V^2 - 0.603V + 0.501$	$V > 0.50$
IWP	$E = E^m$	$0.597V^{1.225}$	$V \leq 0.35$
		$0.987V^{1.782} + 0.013$	$V > 0.35$
	$G = G^m$	$0.529V^{1.287}$	$V \leq 0.35$
		$0.960V^{2.188} + 0.040$	$V > 0.35$
	$v =$	$2.597e^{-0.157V} - 2.244$	$V \leq 0.13$
		$0.201V^2 - 0.227V + 0.326$	$V > 0.13$

The governing equations for free vibration analysis are expressed as follows

$$\int_\Omega \delta\bar{\boldsymbol{\varepsilon}}^T\mathbf{Q}^b\bar{\boldsymbol{\varepsilon}}\mathrm{d}\Omega + \int_\Omega \delta^T\left(\bar{\boldsymbol{\varepsilon}}^s\right)^T\mathbf{Q}^s\bar{\boldsymbol{\varepsilon}}^s\mathrm{d}\Omega + \int_\Omega \delta\bar{\mathbf{u}}^T\mathbf{I}_0\ddot{\mathbf{u}}\mathrm{d}\Omega = \mathbf{0} \tag{10}$$

where $\ddot{\mathbf{u}}$ is acceleration and

$$\bar{\boldsymbol{\varepsilon}} = \left\{ \begin{array}{c} \boldsymbol{\varepsilon}^1 \\ \boldsymbol{\varepsilon}^2 \end{array} \right\};\mathbf{Q}^b = \left[\begin{array}{cc} \mathbf{A}^b & \mathbf{B}^b \\ \mathbf{B}^b & \mathbf{D}^b \end{array} \right];\mathbf{D}^s = \int_{-h/2}^{h/2}\mathbf{C}^s\mathrm{d}z$$

$$\left(\mathbf{A}^b, \mathbf{B}^b, \mathbf{D}^b\right) = \int_{-h/2}^{h/2}\left(1, z, z^2\right)\mathbf{C}^b\mathrm{d}z$$

$$\mathbf{C}^s = \left[\begin{array}{cc} G & 0 \\ 0 & G \end{array} \right];\left(\mathbf{I}_1, \mathbf{I}_2, \mathbf{I}_3\right) = \int_{-h/2}^{h/2}\rho^{TPMS}\left(1, z, z^2\right)\mathbf{I}_{3x3}\mathrm{d}z$$

$$\mathbf{C}^b = \left[\begin{array}{ccc} \frac{E}{1-(\nu)^2} & \frac{\nu E}{1-(\nu)^2} & 0 \\ \frac{\nu E}{1-(\nu)^2} & \frac{E}{1-(\nu)^2} & 0 \\ 0 & 0 & G \end{array} \right];\bar{\mathbf{u}} = \left\{ \begin{array}{c} \mathbf{u}^1 \\ \mathbf{u}^2 \end{array} \right\};\mathbf{I}_0 = \left[\begin{array}{cc} \mathbf{I}_1 & \mathbf{I}_2 \\ \mathbf{I}_2 & \mathbf{I}_3 \end{array} \right] \tag{11}$$

where $\rho = \rho^m \times V$, in which ρ^m is the mass density of base material; $\mathbf{I}_{3\times3}$ is the unit matrix.

2.3. Moving Kriging interpolation shape function for FG-TPMS plates

The mid-plane surface domain of the plate (Ω) can be discretized by a set of nodes $\mathbf{x}_I(I = 1, .., N)$, in which N is the total number of nodes, the displacement field is interpolated by based on a set of nodes

$$\mathbf{u}^h(\mathbf{x}) = \sum_{I=1}^{N} \mathbf{I}_{5\times5} N_I(\mathbf{x}) \mathbf{q}_I \qquad (12)$$

where $\mathbf{q}_I = \left\{ \begin{array}{ccccc} u_I & v_I & w_I & \psi_{xI} & \psi_{yI} \end{array} \right\}^T$ is degrees of freedom (DOFs) of node I; $\mathbf{I}_{5\times5}$ is the unit matrix of 5x5; $N_I(\mathbf{x})$ is the moving Kriging interpolation shape function, which is defined as follows

$$N_I(\mathbf{x}) = \mathbf{p}^T(\mathbf{x})\mathbf{A} + \mathbf{r}^T(\mathbf{x})\mathbf{B} = \sum_{j=1}^{m} p_j(\mathbf{x})A_{jI} + \sum_{k=1}^{n} r_k(\mathbf{x})B_{kI} \qquad (13)$$

in which m and n denote the order of the polynomial basic function and the number of nodes in support domain, respectively.

Additionally, components of $\mathbf{p}(\mathbf{x}), \mathbf{r}(\mathbf{x}), \mathbf{A}$ and $\mathbf{B}$ are formulated by

$$\begin{aligned} \mathbf{p}(\mathbf{x}) &= \left[\begin{array}{cccc} p_1(\mathbf{x}) & p_2(\mathbf{x}) & \cdots & p_m(\mathbf{x}) \end{array} \right]^T \\ \mathbf{r}(\mathbf{x}) &= \left[\begin{array}{cccc} R(\mathbf{x}_1, \mathbf{x}) & R(\mathbf{x}_2, \mathbf{x}) & \cdots & R(\mathbf{x}_n, \mathbf{x}) \end{array} \right]^T \\ \mathbf{A} &= \left(\mathbf{P}^T \mathbf{R}^{-1} \mathbf{P} \right)^{-1} \mathbf{P}^T \mathbf{R}^{-1}; \mathbf{B} = \mathbf{R}^{-1} \left(\mathbf{I} - \mathbf{PA} \right) \end{aligned} \qquad (14)$$

where $\mathbf{I}$ is a unit matrix of size $n \times n$, and

$$\mathbf{P}(\mathbf{x}) = \left[\begin{array}{ccc} p_1(\mathbf{x}_1) & \cdots & p_m(\mathbf{x}_1) \\ \vdots & \ddots & \vdots \\ p_1(\mathbf{x}_n) & \cdots & p_m(\mathbf{x}_n) \end{array} \right]$$

$$\mathbf{R}(\mathbf{x}) = \left[\begin{array}{ccc} R(\mathbf{x}_1, \mathbf{x}_1) & \cdots & R(\mathbf{x}_1, \mathbf{x}_n) \\ \vdots & \ddots & \vdots \\ R(\mathbf{x}_n, \mathbf{x}_1) & \cdots & R(\mathbf{x}_n, \mathbf{x}_n) \end{array} \right] \qquad (15)$$

Components of $\mathbf{p}(\mathbf{x})$ and $R(\mathbf{x}_i, \mathbf{x}_j)$ can be described by

$$\mathbf{p}(\mathbf{x}) = \left\{ \underbrace{\begin{array}{cccccc} 1 & x & y & x^2 & xy & y^2 \end{array}}_{m=6} \right\}^T$$

$$R(\mathbf{x}_i, \mathbf{x}_j) = \exp \left\{ -\left(\frac{\eta}{d_c} \|\mathbf{x}_i - \mathbf{x}_j\| \right)^2 \right\} \qquad (16)$$

where η is a correlation parameter ($\eta = 1$) [28], d_c is the average distance of nodes. And the support domain size of meshfree approximation was investigated in [35].

By substituting Eq. (12) into Eq. (8), bending and shear strains can be formulated by

$$\begin{aligned} \bar{\boldsymbol{\varepsilon}} &= \left\{ \begin{array}{cc} \boldsymbol{\varepsilon}^1 & \boldsymbol{\varepsilon}^2 \end{array} \right\}^T = \sum_{I=1}^{N} \left\{ \begin{array}{cc} \mathbf{B}_I^1 & \mathbf{B}_I^2 \end{array} \right\}^T \mathbf{q}_I = \sum_{I=1}^{N} \bar{\mathbf{B}}_I^b \mathbf{q}_I \\ \boldsymbol{\varepsilon}^s &= \sum_{I=1}^{N} \mathbf{B}_I^s \mathbf{q}_I \end{aligned} \qquad (17)$$

where

$$\begin{aligned} \mathbf{B_I}^1 &= \left[\begin{array}{ccccc} N_{I,x} & 0 & 0 & 0 & 0 \\ 0 & N_{I,y} & 0 & 0 & 0 \\ N_{I,y} & N_{I,x} & 0 & 0 & 0 \end{array} \right. \\ \mathbf{B_I}^2 &= \left. \begin{array}{ccccc} 0 & 0 & 0 & N_{I,x} & 0 \\ 0 & 0 & 0 & 0 & N_{I,y} \\ 0 & 0 & 0 & N_{I,y} & N_{I,x} \end{array} \right] \\ \mathbf{B_I}^s &= \left[\begin{array}{ccccc} 0 & 0 & N_{I,x} & N_I & 0 \\ 0 & 0 & N_{I,y} & 0 & N_I \end{array} \right] \end{aligned} \qquad (18)$$

According to Eq. (6), the displacement field is also described by

$$\bar{\mathbf{u}} = \left\{ \begin{array}{cc} \mathbf{u}^1 & \mathbf{u}^2 \end{array} \right\}^T = \sum_{I=1}^{N} \left\{ \begin{array}{cc} \mathbf{B}_I^{u1} & \mathbf{B}_I^{u2} \end{array} \right\}^T \mathbf{q}_I = \sum_{I=1}^{N} \bar{\mathbf{B}}_I^u \mathbf{q}_I \qquad (19)$$

in which

$$\begin{aligned} \mathbf{B_I}^{u1} &= \left[\begin{array}{ccccc} N_I & 0 & 0 & 0 & 0 \\ 0 & N_I & 0 & 0 & 0 \\ 0 & 0 & N_I & 0 & 0 \end{array} \right. \\ \mathbf{B_I}^{u2} &= \left. \begin{array}{ccccc} 0 & 0 & 0 & N_I & 0 \\ 0 & 0 & 0 & 0 & N_I \\ 0 & 0 & 0 & 0 & 0 \end{array} \right] \end{aligned} \qquad (20)$$

Finally, governing discrete equations for free vibration analysis of FG-TPMS plates are rewriten by inserting Eqs. (17) and (19) into Eq. (10) by

$$\left(\mathbf{K} - \omega^2 \mathbf{M} \right) \bar{\mathbf{q}} = 0 \qquad (21)$$

where $\mathbf{K}$ and $\mathbf{M}$ respectively are the global stiffness matrix and mass matrix that are defined by

$$\mathbf{K} = \int_\Omega \left(\bar{\mathbf{B}}^b\right)^T \mathbf{Q}^b \bar{\mathbf{B}}^b \mathrm{d}\Omega + \int_\Omega \left(\bar{\mathbf{B}}^s\right)^T \mathbf{Q}^s \bar{\mathbf{B}}^s \mathrm{d}\Omega$$
$$\mathbf{M} = \int_\Omega \left(\bar{\mathbf{B}}^u\right)^T \mathbf{I_0} \bar{\mathbf{B}}^u \mathrm{d}\Omega; \mathbf{q} = \bar{\mathbf{q}} e^{i\omega t}$$

(22)

where ω is the natural frequency; $\bar{\mathbf{q}}$ is shape modes.

3.   Numerical validation

This section explores numerical examples for each FG-TPMS plate type, considering six distinct volume distribution scenarios with the corresponding parameters as defined by Eq. (4) and summarized in Table 2. To execute the essential integration for the current meshfree approach, three-node triangular cells are utilized, and integration points (3×3) of the Gaussian quadrature rule are employed for each triangular cell. The properties of the base materials are adopted by $E^m = 200\text{GPa}$, $\rho^m = 8000\text{kg/m}^3$ and $v^m = 0.3$.

3.1.   Square plate

Firstly, an FG-TPMS square plate of length a and thickness h is analyzed under simply supported (SSSS) and fully clamped (CCCC) boundary conditions. The natural frequency of plate is normalized by $\bar{\omega} = \left(\frac{\omega^2 a^4 \rho^m h}{D}\right)^{1/4}$, in which $D = \frac{E^m h^3}{12\left(1-(v^m)^2\right)}$. Table 3 presents the normalized natural frequency of the simply supported FG-TPMS square plate discretized by 498 nodes, corresponding to various TPMS modeled types and volume distribution patterns. These results are compared to those obtained by Nguyen-Xuan et al. [18] using HSDT (5 degrees of freedom (DOFs)) combined to isogeometric analysis. The numerical results are shown in good agreement with the reference values. The findings reveal that the initial non-dimensional natural frequency of Functionally Graded Triply Periodic Minimal Surface (FG-TPMS) square plates exhibits an ascending trend, progressing from the Gyroid type to the Primitive and IWP types in Pattern I. Similarly, in Pattern II, the

trend shifts from Gyroid to IWP and then to Primitive types. Additionally, these frequencies rise proportionally with an increase in the length-to-thickness ratio and decline when transitioning from clamped (CCCC) to simply supported boundaries.

Tab. 2: Various volume distribution patterns with $V_{average} = 0.35$ [18]

Parameter	I1	I2	I3	II1	II2	II3
n	1.0	3.0	6.5	0.561	1.757	3.943
V_{min}	0.2	0.2	0.25	0.1	0.20	0.25
V_{max}	0.5	0.8	1.0	0.5	0.8	1.0

3.2.   Annular plate

An FG-TPMS annular plate with two circles of radii $R_{in} = 0.25$ and $R_{out} = 1$ is considered respectively. The plate is subjected to fully clamped conditions at the outer boundary. For the case of $R_{in} = 0$, the annular plate becomes a circular plate. Figure 2 shows the node distribution of FG-TPMS annular and circular plates. The non-dimensional natural frequency is calculated using the formula by Nguyen-Xuan et al. [18] ($\bar{\Omega} = \omega R_{out}^2 \sqrt{\rho^m h/D}$). Table 4 gives the first non-dimensional natural frequency of fully clamped FG-TPMS circular plate with different ratios of R_{out}/h. The obtained results are compared to the reference ones in [18]. The results obtained are in close agreement with the reference results, showing only minor discrepancies that are not considered significant.

Table 5 presents the first non-dimensional natural frequency of fully clamped FG-TPMS annular plates under various radius-to-thickness ratios, TPMS types, and volume distribution patterns. These results can serve as reference values in future studies, as they are not yet available in the literature. The dominant pattern for the largest natural frequency in fully clamped Functionally Graded Triply Periodic Minimal Surface (FG-TPMS) annular plates is typically identified as the IWP type, while the Gyroid type tends to be associated with the smallest natural frequency. Furthermore, the natural frequency decreases with decreasing radius-to-thickness ratio. Figure 3 depicts the first six shape modes of fully clamped FG-TPMS annular plates.

Tab. 3: The first non-dimensional natural frequency $\bar{\omega}$ of FG-TPMS square plates.

a/h	TPMS	Method	I1	I2	I3	II1	II2	II3
SSSS								
	Primitive	HSDT [18]	3.4826	3.5452	3.7065	3.8517	4.1759	4.1928
		Present	3.4883	3.5545	3.7230	3.8698	4.2177	4.2277
10	Gyroid	HSDT [18]	3.4047	3.4726	3.6638	3.7183	4.0429	4.0891
		Present	3.4120	3.4867	3.6876	3.7422	4.1036	4.1427
	IWP	HSDT [18]	3.5188	3.6009	3.7639	3.8131	4.1210	4.1490
		Present	3.5279	3.6194	3.7937	3.8399	4.1880	4.2091
	Primitive	HSDT [18]	3.5274	3.5965	3.7735	3.9322	4.3050	4.3148
		Present	3.5479	3.6166	3.7932	3.9485	4.3191	4.3290
200	Gyroid	HSDT [18]	3.4553	3.5317	3.7455	3.8090	4.1968	4.2384
		Present	3.4723	3.5491	3.7609	3.8234	4.2099	4.2509
	IWP	HSDT [18]	3.5811	3.6733	3.8603	3.9206	4.2951	4.3161
		Present	3.5952	3.6884	3.8741	3.9319	4.3060	4.3272
CCCC								
	Primitive	HSDT [18]	4.4454	4.5076	4.6924	4.9193	5.2988	5.3386
		Present	4.4627	4.5375	4.7426	4.9740	5.4244	5.4412
10	Gyroid	HSDT [18]	4.4413	4.5241	4.7343	4.7741	5.1064	5.1814
		Present	4.4609	4.5699	4.8117	4.8459	5.2888	5.3415
	IWP	HSDT [18]	4.6490	4.7339	4.8999	4.9511	5.2322	5.2746
		Present	4.6735	4.7946	4.9981	5.0343	5.4372	5.4570
	Primitive	HSDT [18]	4.5914	4.6724	4.9064	5.1894	5.7319	5.7507
		Present	4.6798	4.7610	4.9913	5.2588	5.7924	5.8111
200	Gyroid	HSDT [18]	4.6208	4.7332	5.0212	5.0902	5.6285	5.6928
		Present	4.6887	4.8029	5.0843	5.1483	5.6820	5.7450
	IWP	HSDT [18]	4.8852	5.0055	5.2551	5.3478	5.8442	5.8634
		Present	4.9409	5.0646	5.3104	5.3957	5.8909	5.9105

Tab. 4: The natural frequencies of the fully clamped FG-TPMS circular plates.

R_{out}/h	TPMS	I1		I2		I3	
		Ref [18]	Present	Ref [18]	Present	Ref [18]	Present
	Primitive	6.0679	6.0741	6.2887	6.2926	6.9333	6.9453
50	Gyroid	6.0993	6.1004	6.3954	6.3967	7.1948	7.1938
	IWP	6.7852	6.7826	7.1244	7.1235	7.8522	7.8502
	Primitive	5.7100	5.7175	5.8759	5.9168	6.3677	6.4652
5	Gyroid	5.6468	5.6707	5.8537	5.9468	6.4066	6.5935
	IWP	6.1469	6.1904	6.3731	6.5171	6.8237	7.0830

4.   Conclusions

This study analyzed the free vibration behavior of FG-TPMS plates using the numerical model, which seamlessly integrates first-order shear deformation theory and the moving Kriging meshfree method. The study was encompassed three distinct TPMS structures (Primitive, Gyroid, and IWP) and six volume distribution patterns for each pattern. To accurately determine the mechanical properties of FG-TPMS materials, a fitting technique employing a two-phase piecewise function was employed. The obtained results from the present meshfree model were exhibited remarkable agreement with the original reference results obtained via isogeometric analysis. Key observations gleaned from numerical examples are summarized by: i) The natural fre-

Tab. 5: The first normalized natural frequency of the fully clamped FG-TPMS annular plates with different radius-to-thickness ratio.

R_{out}/h	TPMS	I1	I2	I3
50	Primitive	6.5759	6.8181	7.5190
	Gyroid	6.4772	6.7796	7.6230
	IWP	7.1388	7.4963	8.2652
10	Primitive	6.4359	6.6704	7.3403
	Gyroid	6.3219	6.6153	7.4160
	IWP	6.9418	7.2916	8.0144
5	Primitive	6.1662	6.3837	6.9719
	Gyroid	6.0097	6.2873	6.9787
	IWP	6.5243	6.8619	7.4706
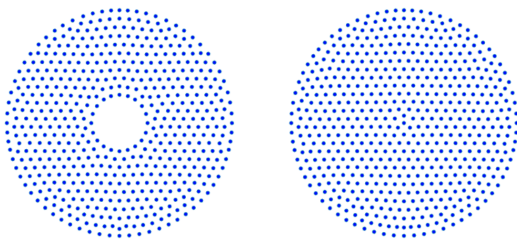
Fig. 2: Node distributions of FG-TPMS annular and circular plates.
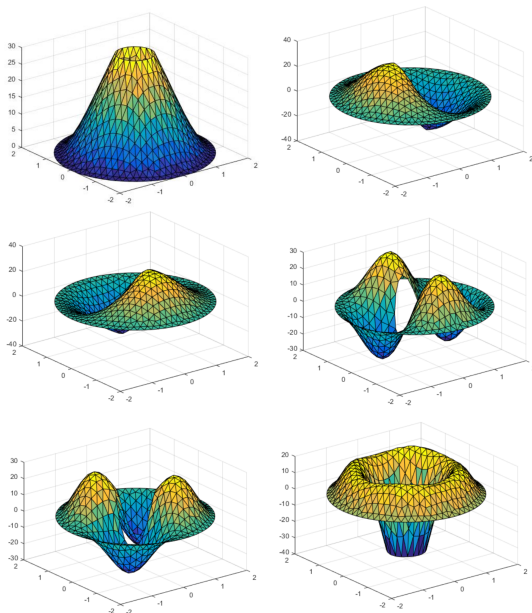
Fig. 3: The first six shape modes of fully clamped FG-TPMS annular plates (IWP, R_{out}/h =5).

quency exhibits a decreasing trend from lowest to highest for Gyroid, Primitive, and IWP types with the pattern I and from Gyroid, IWP, and Primitive types with the pattern II; ii) The natural frequency yielded by the pattern I are lower than those of the pattern II; iii) An increase in the length-to-thickness ratio and a transition from simply supported to fully clamped boundaries lead to an increase in both the natural frequency.

References

[1] Liu, M. (2005). Dynamic crushing of 2D cellular structures: A finite element study. *International Journal of Impact Engineering*, *32*, 650–664.

[2] Sun, Y. & Li, Q. (2018). Dynamic compressive behaviour of cellular materials: A review of phenomenon, mechanism and modelling. *International Journal of Impact Engineering*, *112*, 74–115.

[3] Maskery, I., Sturm, L., Aremu, A., Panesar, A., Williams, C., Tuck, C., Wildman, R., Ashcroft, I., & Hague, R. (2018). Insights into the mechanical properties of several triply periodic minimal surface lattice structures made by polymer additive manufacturing. *Polymer*, *152*, 62–71.

[4] Al-Ketan, O., Lee, D., Rowshan, R., & Al-Rub, R. (2020). Functionally graded and multi-morphology sheet TPMS lattices: Design, manufacturing, and mechanical properties. *Journal of the Mechanical Behavior of Biomedical Materials*, *102*, 103520.

[5] Novak, N., Al-Ketan, O., Borovinšek, M., Krstulović-Opara, L., Rowshan, R., Vesenjak, M., & Ren, Z. (2021). Development of novel hybrid TPMS cellular lattices and their mechanical characterisation. *Journal of Materials Research and Technology*, *15*, 1318–1329.

[6] Afshar, M., Anaraki, A., Montazerian, H., & Kadkhodapour, J. (2016). Additive manufacturing and mechanical characterization of graded porosity scaffolds designed based

on triply periodic minimal surface architectures. *Journal of the Mechanical Behavior of Biomedical Materials*, *62*, 481–494.

[7] Cheng, L., Bai, J., & To, A. (2019). Functionally graded lattice structure topology optimization for the design of additive manufactured components with stress constraints. *Computer Methods in Applied Mechanics and Engineering*, *344*, 334–359.

[8] Melchels, F., Bertoldi, K., Gabbrielli, R., Velders, A., Feijen, J., & Grijpma, D. (2010). Mathematically defined tissue engineering scaffold architectures prepared by stereolithography. *Biomaterials*, *31*, 6909–6916.

[9] Zhao, M., Zhang, D., Liu, F., Li, Z., Ma, Z., & Ren, Z. (2020). Mechanical and energy absorption characteristics of additively manufactured functionally graded sheet lattice structures with minimal surfaces. *International Journal of Mechanical Sciences*, *167*, 105262.

[10] Zhang, C., Jiang, Z., Zhao, L., Guo, W., Jiang, Z., Li, X., & Chen, G. (2021). Mechanical characteristics and deformation mechanism of functionally graded triply periodic minimal surface structures fabricated using stereolithography. *International Journal of Mechanical Sciences*, *208*, 106679.

[11] Yang, L., Mertens, R., Ferrucci, M., Yan, C., Shi, Y., & Yang, S. (2019). Continuous graded Gyroid cellular structures fabricated by selective laser melting: Design, manufacturing and mechanical properties. *Materials & Design*, *162*, 394–404.

[12] Ma, S., Song, K., Lan, J., & Ma, L. (2020). Biological and mechanical property analysis for designed heterogeneous porous scaffolds based on the refined TPMS. *Journal of the Mechanical Behavior of Biomedical Materials*, *107*, 103727.

[13] Wang, S., Shi, Z., Liu, L., Zhou, X., Zhu, L., & Hao, Y. (2020). The design of Ti6Al4V Primitive surface structure with symmetrical gradient of pore size in

biomimetic bone scaffold. *Materials & Design*, *193*, 108830.

[14] Keshavarzan, M., Kadkhodaei, M., Badrossamay, M., & Ravari, M. (2020). Investigation on the failure mechanism of triply periodic minimal surface cellular structures fabricated by Vat photopolymerization additive manufacturing under compressive loadings. *Mechanics of Materials*, *140*, 103150.

[15] Afshar, M., Anaraki, A.P., & Montazerian, H. (2018). Compressive characteristics of radially graded porosity scaffolds architectured with minimal surfaces. *Materials Science and Engineering: C*, *92*, 254–267.

[16] Qiu, N., Zhang, J., Li, C., Shen, Y., & Fang, J. (2023). Mechanical properties of three-dimensional functionally graded TPMS structures. *International Journal of Mechanical Sciences*, *246*, 108118.

[17] Viet, N. & Zaki, W. (2021). Free vibration and buckling characteristics of functionally graded beams with triply periodic minimal surface architecture. *Composite Structures*, *274*, 114342.

[18] Nguyen-Xuan, H., Tran, K., Thai, C., & Lee, J. (2023). Modelling of functionally graded triply periodic minimal surface (FG-TPMS) plates. *Composite Structures*, *315*, 116981.

[19] Nguyen, N., Tran, K., Phung-Van, P., Lee, J., & Nguyen-Xuan, H. (2023). An isogeometric analysis of functionally graded triply periodic minimal surface microplates. *Aerospace Science and Technology*, *137*, 108270.

[20] Bazilevs, Y., Takizawa, K., Hsu, M.C., Tezduyar, T., Otoguro, Y., Mochizuki, H., & Wu, M. (2020). Wind turbine and turbomachinery computational analysis with the ALE and space-time variational multiscale methods and isogeometric discretization. *Journal of Advanced Engineering and Computation*, *4*, 1–32.

[21] Hung, P., Nguyen-Thanh, T., Phung-Van, P., & Nguyen-Gia, H. (2023). Isogeometric vibration of the magneto-electro-elastic sandwich plate with functionally graded carbon nanotube reinforced composite core. *Journal of Advanced Engineering and Computation, 7*, 187–203.

[22] Takizawa, K., Bazilevs, Y., Tezduyar, T., Hsu, M.C., & Terahara, T. (2022). Computational cardiovascular medicine with isogeometric analysis. *Journal of Advanced Engineering and Computation, 6*, 167–199.

[23] Zhang, Y., Ren, H., & Rabczuk, T. (2022). Nonlocal Operator Method for Solving Partial Differential Equations: State-of-the-Art Review and Future Perspectives. *Journal of Advanced Engineering and Computation, 6*, 1–35.

[24] Gu, L. (2003). Moving kriging interpolation and element-free Galerkin method. *International Journal for Numerical Methods in Engineering, 56*, 1–11.

[25] Thai, C., Do, V., & Nguyen-Xuan, H. (2016). Computational Cardiovascular Medicine With Isogeometric Analysis. *Engineering Analysis with Boundary Elements, 64*, 122–136.

[26] Nguyen, T., Thai, C., & Nguyen-Xuan, H. (2016). A novel computational approach for functionally graded isotropic and sandwich plate structures based on a rotation-free meshfree method. *Thin-Walled Structures, 107*, 473–488.

[27] Thai, C., Nguyen, T., Rabczuk, T., & Nguyen-Xuan, H. (2016). An improved moving Kriging meshfree method for plate analysis using a refined plate theory. *Computers & Structures, 176*, 34–49.

[28] Thai, C., Ferreira, A., & Nguyen-Xuan, H. (2017). Naturally stabilized nodal integration meshfree formulations for analysis of laminated composite and sandwich plates. *Composite Structures, 178*, 260–276.

[29] Thai, C., Ferreira, A., Rabczuk, T., & Nguyen-Xuan, H. (2018). A naturally stabilized nodal integration meshfree formula-

tion for carbon nanotube-reinforced composite plate analysis. *Engineering Analysis with Boundary Elementss, 92*, 136–155.

[30] Hung, P., Thai, C., & Phung-Van, P. (2023). A C0-HSDT free vibration of magneto-electro-elastic functionally graded porous plates using a moving Kriging meshfree method. *Aerospace Science and Technology, 137*, 108266.

[31] Nguyen, L., Thai, C., & Nguyen-Xuan, H. (2023). A Moving Kriging Meshfree Method for The Vibration Analysis of Homogenous Magneto-electro-elastic Plates. *Journal of Advanced Engineering and Computation, 7*, 31–41.

[32] Thai, C., Tran, T., & Phung-van, P. (2020). A size-dependent moving Kriging meshfree model for deformation and free vibration analysis of functionally graded carbon nanotube-reinforced composite nanoplates. *Engineering Analysis with Boundary Elements, 115*, 52–63.

[33] Thai, C., Ferreira, A., Lee, J., & Nguyen-Xuan, H. (2018). An efficient size-dependent computational approach for functionally graded isotropic and sandwich microplates based on modified couple stress theory and moving Kriging-based meshfree method. *International Journal of Mechanical Sciences, 142–143*, 322–338.

[34] Thai, C., Nguyen-Xuan, H., Nguyen, L., & Phung-Van, P. (2022). A modified strain gradient meshfree approach for functionally graded microplates. *Engineering with Computers, 38*, 4545–4567.

[35] Thai, C., Do, V., & Nguyen-Xuan, H. (2016). An improved Moving Kriging-based meshfree method for static, dynamic and buckling analyses of functionally graded isotropic and sandwich plates. *Engineering Analysis with Boundary Elements, 64*, 122–136.

About Authors

Phuc Van PHUNG received his Ph.D from Ghent University in 2016. He has been conducting computational mechanics research since 2012. Currently, he is a senior lecturer at the Faculty of Civil Engineering, HUTECH University, Ho Chi Minh City, Vietnam. He has published over 58 Web-of-Science-indexed journal articles on computational and structural mechanics and nanostructures. He is one of World's Best Mechanical and Aerospace Engineering Scientists according to Research.com. He is also one of Best Rising Stars of Science in the World - 2022.

Hung Tan PHAM was born in Vietnam in 1981. He has a Ph.D. degree in Mechanics. Now, he is a lecturer at the Faculty of Civil Engineering at Ho Chi Minh City University of Technology and Education, Ho Chi Minh City, Vietnam. His research interests are the computational mechanics.

Huy Gia NGUYEN was born in Vietnam in 1993. He has a M.EnG in Civil Engineering. Now, he is working at Ho Chi Minh City University of Technology (HUTECH University), Ho Chi Minh City, Vietnam.

H. NGUYEN-XUAN received his Ph.D. in Computational Mechanics from the University of Liège (Belgium) in 2008. His current research focuses on computational engineering, applied mathematics, data-driven machine learning methodology, 3D printing and hydrogen energy. Dr. Nguyen-Xuan has carried out significant research collaborations with leading research institutions and universities around the world. The national and international cooperation in research has been providing him widespread recognition in the field of computational mechanics. He has published more than 250 peer-reviewed articles.